RESEARCH ARTICLE

60 years of pss

physica status solidi rrl

www.pss-rapid.com

Partial Auxeticity of Laterally Compressed Carbon Nanotube Bundles

Elena A. Korznikova, Kun Zhou, Leysan Kh. Galiakhmetova, Elvira G. Soboleva, Aleksey A. Kudreyko, and Sergey V. Dmitriev*

Carbon nanotubes (CNTs) have attracted increasing attention because of their enormous potential in various technologies. Herein, the evolution of the structure and elastic properties of a CNT bundle under compression in uniaxial and biaxial regimes is analyzed using a chain model with a reduced number of degrees of freedom. The compression stress–strain curves consist of four stages, each of which is characterized by a specific structure and deformation mechanism. In the first stage, all CNTs have the same cross section; in the second stage, the translational symmetry is preserved in the system, but with a doubled translational cell; in the third stage, CNT collapse takes place, leading to the loss of the translational symmetry; the fourth stage begins when all CNTs collapse. Elastic constants are calculated for the CNT bundle under uniaxial and biaxial compression during the first two stages. In all loading schemes, during the second stage of deformation, the CNT bundle exhibits partial auxetic properties. The results obtained contribute to the fundamental knowledge for the design of carbon nanomaterials with enhanced properties.

1. Introduction

Carbon nanotubes (CNTs) discovered in 1991 by Iijima[1] demonstrated outstanding mechanical properties with the tensile strength higher than 100 GPa and Young's modulus over 1 TPa.[2] Despite the fact that their actual strength is an order of magnitude lower than the theoretically predicted value, due to the inevitable defects,[3] for almost 30 years, they have been recognized as the strongest material ever known. The unique combination of properties makes CNTs an ideal candidate to be applied in artificial muscles,[4] drug delivery,[5] resonators,[6] space elevator projects,[7] energy storage and harvesting,[8,9] etc. Another important advantage of CNTs is their relatively facile fabrication to obtain a wide range of geometric characteristics (diameter, length, and chirality)[10,11] that can be extrapolated to the synthesis of CNT bundles.[12,13] The material of this type, also called a forest or an array of CNTs, has even higher mechanical properties than individual nanotubes, because of the van der Waals interactions between them.[14] In the study by Karimzad Ghavidel et al.,[15] the mechanical properties of CNT bundles aligned in a liquid medium using an external electric field were studied theoretically and experimentally.

The success in the production and analysis of CNTs inspires the creation of nanotubes from other recently discovered 2D materials.[16–21]

The low flexural rigidity of sp^2 carbon nanostructures determines the main mechanism of their deformation, a change in valence bond angles and dihedral angles, whereas the contribution from a change in the length of covalent bonds remains small. This was demonstrated for CNTs subject to twisting[22] and lateral compression,[23] as well as for wrinkled, twisted, and scrolled graphene nanoribbons.[24–28] In the study by

E. A. Korznikova, L. K. Galiakhmetova, S. V. Dmitriev
Institute for Metals Superplasticity Problems
RAS
450001 Ufa, Russia

E. A. Korznikova
Department of Materials Science and Physics of Metals
Ufa State Aviation Technical University
450008 Ufa, Russia

K. Zhou
School of Mechanical and Aerospace Engineering
Nanyang Technological University
50 Nanyang Avenue, Singapore 639798, Singapore
E-mail: kzhou@ntu.edu.sg

E. G. Soboleva
Yurga Institute of Technology (Branch)
National Research Tomsk Polytechnic University
652050 Yurga, Russia

A. A. Kudreyko
Department of Medical Physics and Informatics
Bashkir State Medical University
450008 Ufa, Russia

S. V. Dmitriev
Federal Research Center
The Institute of Applied Physics of RAS
603950 Nizhny Novgorod, Russia

The ORCID identification number(s) for the author(s) of this article can be found under https://doi.org/10.1002/pssr.202100189.

DOI: 10.1002/pssr.202100189

Elliott et al.,[29] it was found that the CNT collapse pressure does not depend on the chirality of the nanotubes but strongly depends on their diameter, whereas their collapse can increase the strength by up to 30 %. Since then many attempts have been made to find the architecture of CNT bundles with optimal mechanical properties. Thus, in the study by Cheng et al.,[30] it was shown that the volume of the CNT bundle can be controlled by the application of the external electric field. According to the study by Silva-Santos et al.,[31] the collapse pressure of multiwalled CNTs depends essentially on both the number of tube walls and the innermost diameter. A possibility to reach the strength up to 3–6 GPa and Young's modulus up to 200–350 GPa for CNT arrays and fibers was demonstrated in the study by Zhang et al.,[32] whereas the dynamical performance was reported to depend strongly on the nanotube interface distance, alignment, packing density, aggregation size, and other parameters. The enhanced stability of bundles was attained when the innermost diameter was smaller than 1.5 nm because of the bundle intertube geometry-induced interactions.[33]

Because of their small size and reduced dimensionality, CNTs can be effectively studied using computer simulations.[34,35] Among the most common approaches, one can recall the continuum shell models,[22,36,37] membrane spring model,[38,39] molecular structure mechanics,[40,41] coarse-grained approach,[42] and classical molecular dynamics (MD) simulations.[23,43,44] CNT bundles under a tensile load can be modeled assuming that nanotubes are rigid.[45] The MD method is the most popular one because of its versatility and availability, which in turn has made it possible to obtain a number of important results. A disadvantage of the MD method in the study of CNT bundles is the need to consider a large number of degrees of freedom that requires large-scale computations. Models with a reduced number of degrees of freedom have been developed.[46] This work deals with a chain model moving on a plane that was earlier shown to be an effective tool for the consideration of carbon nanoscrolls,[47] windings of graphene nanoribbons around CNTs,[48] lateral compression of CNT bundles,[49–52] dynamics of ripplocations[53] and rotobreathers,[54] and eigenfrequencies of bending vibrations of CNTs.[55]

Materials with complex structural elements, such as particles with rotational degrees of freedom, often exhibit anomalous mechanical and physical properties, for example, negative Poisson's ratios, negative thermal expansion, or negative compressibility.[56–58] CNT bundles under lateral plane strain compression can be regarded as a nanomaterial composed of highly deformable elements (circular cross sections of CNTs), and it seems important to study their mechanical properties.

Materials with negative Poisson's ratios are called auxetics,[59] which expand laterally under uniaxial tension. There are many carbon nanomaterials, such as porous graphene structures,[60] covalently connected CNT networks,[61–65] fullerene nanotube nanotruss networks,[66] wrinkled graphene due to the presence of vacancies,[67] CNT heterojunctions,[68] CNT sheets (buckypaper),[69–71] and diamond-like phases,[72–74] with such auxetic properties. CNTs are used as reinforcing elements in the composites with auxetic properties.[75–79] The auxeticity of nano-/microtubes produced from orthorhombic crystals has been reported in the study by Goldstein et al.[80]

The auxetic behavior can be demonstrated by macroscopic tubular structures[81] as well as microscopic and nanoscopic structures.[80–83] It was observed in the all-electron ab initio study for the short, capped (9,0) CNTs due to endcap effects.[84] Defected CNTs exhibit auxetic behavior and can be used to improve the pullout energy in a CNT–polyethylene composite via the auxetic effect.[75,85,86]

Most of the works devoted to the evolution of the structure of a CNT array under pressure report a similar sequence of steps, which has been confirmed experimentally,[87] namely, polygonization, collapse, and rearrangement of dog-bone components. The deformation at each step depends on the initial configuration and on the type of loading. In contrast, the evolution of the mechanical properties of CNT bundles has not been carefully studied.

In our previous works on the lateral compression of CNT bundles, the chain model was developed,[49] the damping properties of the bundles were analyzed,[50] and the structural characteristics of the CNT bundles under biaxial compression were reported.[51]

The aim of the present work is to conduct a detailed analysis on the mechanical properties of the CNT bundles under plane strain lateral compression.

In Section 2, the simulation model is described. Numerical results are presented in Section 3. In particular, after the description of the CNT bundle structure evolution in Section 3.1, the stress–strain curves are described in Section 3.2 and the elastic constants in Section 3.3. The deformation mechanisms are analyzed in Section 3.4. The discussion of the results and conclusions are given in Section 4.

2. Simulation Setup

In this study, we consider the uniaxial and biaxial plane strain compression of a bundle of CNTs. The nanotubes are oriented along the z-axis and their circular cross sections form a close-packed triangular lattice in the xy-plane with a close-packed direction along the x-axis; see **Figure 1**.

The zigzag CNTs having a diameter D are considered. A considerable reduction of the number of degrees of freedom is achieved by assuming that each carbon atom of the CNT cross

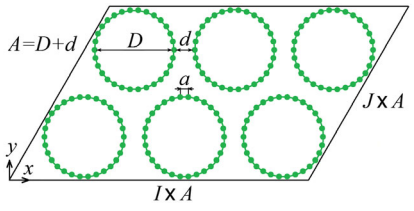

Figure 1. Geometry of the CNT bundle with $I \times J$ nanotubes ($I = 3, J = 2$ in this plot, whereas $I = 10, J = 12$ is used in the simulations). Each zigzag CNT is represented by 30 carbon atoms that move on the xy-plane. a is the distance in the xy-plane between carbon atoms in the CNT wall, d is the distance between the walls of the adjacent CNTs, D is the CNT diameter, and $A = D + d$ is the distance between the centers of adjacent CNTs. The length values of the sides of the computational cell in the form of a parallelogram are $I \times A$ and $J \times A$. The computational cell is subject to the periodic boundary conditions.

section represents the whole atomic row parallel to the CNT axis (z-axis), which moves as a rigid body and has two degrees of freedom—the components of the displacement vector in the xy-plane. In Figure 1, the geometry parameters of the CNT bundle are specified: the distance in the xy-plane between neighboring carbon atoms in the CNT wall is a; the distance between the walls of the adjacent nanotubes is d; $A = D + d$ is the distance between centers of the adjacent nanotubes. For most simulations, the computational cell includes an array of 10×12 CNTs (the case of 3×2 CNTs is shown in Figure 1). Each CNT cross section is represented by 30 atoms, and the total number of atoms in the computational cell is $N = 10 \times 12 \times 30 = 3600$. To demonstrate the effect of the computational cell size, for the biaxial compression case, we present the results for a cell with 20×24 CNTs (double in the size in the x- and y-axis compared with the cell with 10×12 CNTs).

We note that similar reduction of degrees of freedom can be achieved for the armchair CNTs or for chiral CNTs with not very large chiral indices. We believe that the effects observed in this work are associated with a large difference in the bending and tensile stiffness of the CNT wall, which is retained for CNTs of any chirality; hence, the chirality should not be a critical factor. With this in mind, we only consider the case of zigzag CNTs. In the future, we plan to analyze the effect of chirality, which can give quantitative changes in the results.

The equilibrium interatomic distance in graphene is $\rho = 1.418$ Å. The equilibrium distance between adjacent rigid atomic rows oriented along the z-axis is $a = \rho\sqrt{3}/2 = 1.228$ Å, the diameter of the nanotube is $D = 30a/\pi = 11.73$ Å, the equilibrium distance between adjacent CNT walls under zero pressure is $d = 3.088$ Å, and the distance between the centers of neighboring CNTs can be found as $A = D + d = 14.838$ Å. Periodic boundary conditions in both directions are used. In our simulations the units of distance, energy, and time are Å, eV, and ps, respectively. Using these units, the mass of the carbon atom can be found as $M = 12 \times 1.0364 \times 10^{-4}$ eV ps^2 Å^{-2}.

The dynamics of the CNT bundle is described by the Hamiltonian (total energy)[47,49]

$$H = K + U_B + U_A + U_{vdW} \tag{1}$$

where the four terms in the right-hand side give the kinetic energy of the system, energy of valence bonds, energy of valence angles, and energy of van der Waals interactions, respectively. The recipes for calculating these four types of energies are described in detail in our open-access work[49] and are not reproduced here. The model has been successfully used to describe the structure and peculiar mechanical properties of CNT bundles and other carbon 2D materials.[46,48,50–54]

Step-wise, strain-controlled loading with structure relaxation after each increment of strain is conducted. This means that perturbation–relaxation MD is used and thermal vibrations are not taken into account. In other words, the study is focused on the analysis of equilibrium structures at 0 K obtained under deformation instead of force loading. Uniaxial compression along x-axis (y-axis) is achieved by applying increments of homogeneous stain $\Delta\varepsilon_{xx} = -0.01$ ($\Delta\varepsilon_{yy} = -0.01$) to the computational cell, whereas in the biaxial compression $\Delta\varepsilon_{xx} = \Delta\varepsilon_{yy} = -0.01$ is used. In all cases, $\Delta\varepsilon_{zz} = 0$. The deformed state of the structure in all cases is characterized by the absolute value of volumetric strain.

$$|\theta| = |\varepsilon_{xx} + \varepsilon_{yy}| \tag{2}$$

where ε_{xx} and ε_{yy} are the accumulated strain components.

Using the perturbation–relaxation algorithm, the simulations are conducted as follows. Each increment of homogeneous strain is followed by the perturbation of atomic coordinates by adding random displacements distributed uniformly over the range from -10^{-6} to 10^{-6} Å. After that, the potential energy of the system is minimized using the conjugate gradient method and the equilibrium structure is obtained. Energy minimization is conducted until the absolute value of the maximum atomic force becomes smaller than 10^{-10} eV Å^{-1}.

The use of relaxation dynamics means that thermal fluctuations are not taken into account or in other words, the simulation temperature is $T = 0$.

In our work, we present the tangential elastic properties, which are calculated by applying small strains around the strain level achieved in small increments, followed by the structure relaxation. In this case, the linear theory of elasticity works well.

Hooke's law for plane strain is taken in the form

$$\begin{pmatrix} \sigma_{xx} \\ \sigma_{yy} \\ \sigma_{xy} \end{pmatrix} = \begin{pmatrix} C_{11} & C_{12} & C_{13} \\ C_{21} & C_{22} & C_{23} \\ C_{31} & C_{32} & C_{33} \end{pmatrix} \begin{pmatrix} \varepsilon_{xx} \\ \varepsilon_{yy} \\ \varepsilon_{xy} \end{pmatrix} \tag{3}$$

where C_{ij} are the coefficients of the stiffness matrix.

We use the well-known approach[88] for estimating the tangent elastic constants by calculating the average stress values for the incremental strain components including $(\varepsilon_{xx}, \varepsilon_{yy}, \varepsilon_{xy}) = (\pm\xi, 0, 0)$, $(\varepsilon_{xx}, \varepsilon_{yy}, \varepsilon_{xy}) = (0, \pm\xi, 0)$, and $(\varepsilon_{xx}, \varepsilon_{yy}, \varepsilon_{xy}) = (0, 0, \pm\xi)$ and average C_{ij} values calculated for positive and negative ξ. In our simulations, practically the same result was obtained for $10^{-3} \le \xi \le 10^{-7}$. We take the value $\xi = 10^{-7}$ to minimize the effect of anisotropy introduced by the lattice strain.

The tangent engineering elastic constants can be found as follows.

$$\nu_{xy} = C_{21}/C_{22}, \quad \nu_{yx} = C_{12}/C_{11}, \quad G_{xy} = C_{33} \tag{4}$$

$$E_{xx} = C_{11}(1 - \nu_{xy}\nu_{yx}), \quad E_{yy} = C_{22}(1 - \nu_{xy}\nu_{yx}) \tag{5}$$

where ν_{xy} and ν_{yx} are Poisson's ratios, G_{xy} is the tangent shear modulus, and E_{xx} and E_{yy} are the tangent Young's moduli along the x- and y-axis, respectively.

3. Simulation Results

The evolution of the CNT bundle structure is first described; then, the stress–strain curves and elastic constants are presented as the functions of volumetric strain for uniaxial and biaxial compression.

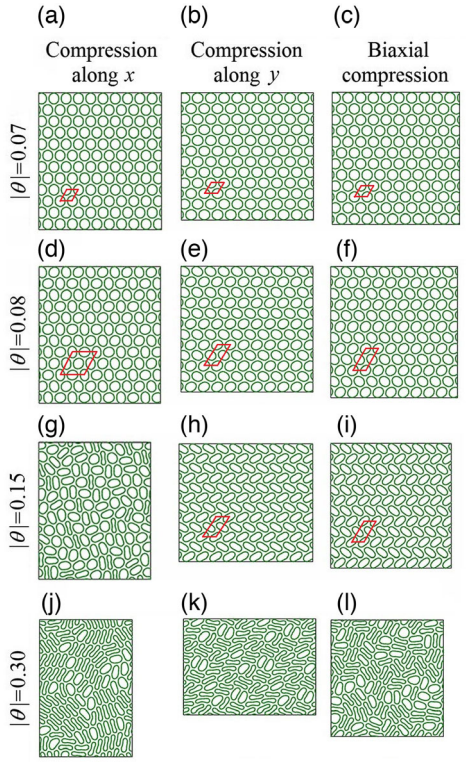

Figure 2. Structure evolution of the CNT bundle under compression along the *x*-axis (the left column) and along the *y*-axis (the middle column) and biaxial compression (the right column). The volumetric strain values are indicated for each row. For structures with translational symmetry, the red lines show the translation cells.

3.1. Evolution of the Structure

Figure 2 shows the evolution of the structure of the compressed CNT bundle. The left column is for compression along *x*-axis, the middle column for compression along *y*-axis, and the right column for biaxial compression. For each row, the absolute value of the volumetric strain is indicated, which increases from top to bottom. For the structures with translational symmetry, translation cells are shown by the red lines.

In the first row, for $|\theta| = 0.07$, one can see structures with the translational symmetry where all CNTs have the same cross section for each loading scheme. In (a) and (b), the CNTs are in elliptical shape elongated in vertical and horizontal directions, respectively. In (c), the CNTs are slightly polygonized, which can hardly be seen in the scale of the figure.

For $|\theta| = 0.08$ in the second row of Figure 2, a qualitative change in the structure can be observed for all three loading schemes. Translational symmetry is preserved in all cases, but the size of the translation cells differs from that in the case $|\theta| = 0.07$. In (d), for compression along the *x*-axis, the translation cell doubles along two directions and includes four CNTs, whereas in (e) and (f), the period doubles in one direction and the translation cell includes two CNTs. In the case of a computational cell with odd *I* and/or *J*, one can expect the formation of domains of structures separated by domain walls.

The further increase in compressive strain leads to gradual collapse of nanotubes that reach the saturation at strain slightly above $|\theta| = 0.30$, when all CNTs collapse. For compression along the *x*-axis, collapsed CNTs appear at $|\theta| = 0.124$ and can be seen in (g) at $|\theta| = 0.15$. In (h) and (i), at $|\theta| = 0.15$, the translational symmetry is still preserved, as for compression along the *y*-axis, the CNT collapse starts at $|\theta| = 0.178$ and for biaxial compression it starts at $|\theta| = 0.151$.

The last row in Figure 2 shows the structures at $|\theta| = 0.30$, in which the fraction of the remaining uncollapsed CNTs is small.

3.2. Compressive Stress–Strain Curves

Figure 3 shows the compressive stress–strain curves $-\sigma_{xx}(|\theta|)$ (the black lines) and $-\sigma_{yy}(|\theta|)$ (the red lines) for (a) compression

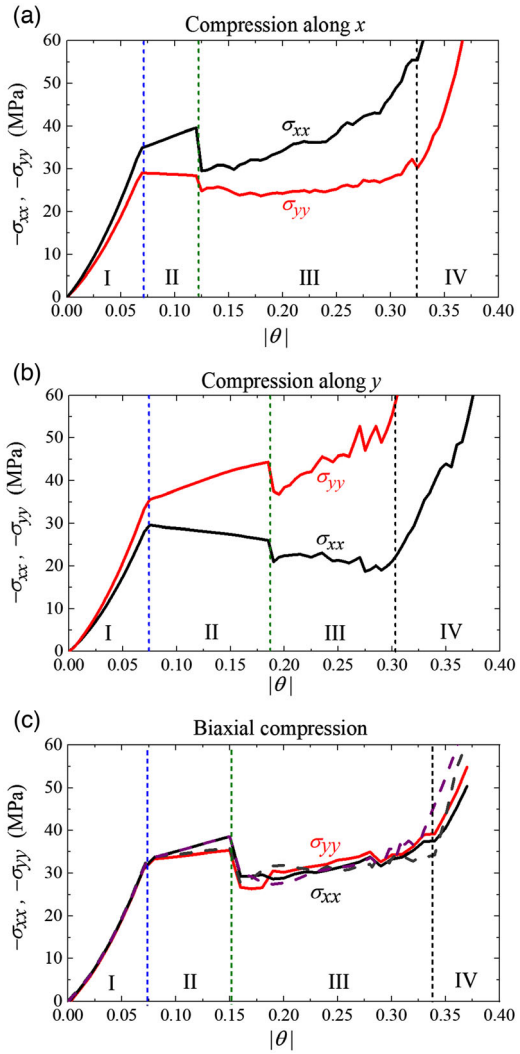

Figure 3. a–c) Components of normal stress as the functions of the volumetric compressive strain during compression along the *x*-axis (a), along the *y*-axis (b), and for biaxial compression (c). The black (red) lines show σ_{xx} (σ_{yy}). Vertical dashed lines separate four stages of deformation numbered from I to IV. Shear stress is not plotted as it is very small in all cases.

along the x-axis, (b) compression along the y-axis, and (c) biaxial compression. In (c), the solid (dashed) lines present the results for small (large) computational cell. The shear stress σ_{xy} is not shown because in all cases it is at least an order of magnitude smaller than the normal stresses. For all loading schemes, the stress–strain curves feature four stages, reflecting the evolution of the CNT bundle structure; see Section 3.1. The vertical lines separate the stages numbered with Roman numerals from I to IV.

Stage I is up to about $|\theta| = 0.07$ with no qualitative changes in the CNT bundle structure; see the first row of Figure 2. Within this stage, the compressive stresses grow rapidly with the strain. In (a) and (b), within stage I, the compressive stress along the loading direction is only slightly higher than that in the transverse direction, which means that one can expect a value of Poisson's ratio close to 1. The result will be confirmed in the following section. In (c), within stage I, $\sigma_{xx} = \sigma_{yy}$ because of the isotropy of the regular structure under biaxial compression.

The transition from stage I to stage II is accompanied by a sharp change in the slope of the stress–strain curves, but there is no discontinuity at the transition point. The structures with a translation cell having a single CNT transform into periodic structures with the doubled translation cells; see the second row of Figure 2. The stress–strain curves within stage II are linear. Interestingly, in (a) and (b), the uniaxial compression results in the reduction of the normal compressive strain in the lateral direction, namely, σ_{yy} in (a) and σ_{xx} in (b) decrease. In (c), σ_{xx} increases with the strain faster than σ_{yy}.

At the transition point from stage II to stage III, a sharp drop of the normal compressive stresses takes place for all loading schemes. At this point, collapsed CNTs appear in the structure, which was described earlier.[50,51] The further increase in volumetric strain within stage III results in the gradual increase in the fraction of collapsed CNTs; see the last row of Figure 2. Stage IV begins when all CNTs collapse.

The effect of the size of the computational cell is discussed by comparing the solid and dashed lines in Figure 3c obtained for the small and large cells, respectively. Within stages I and II, the results obtained for computational cells of different sizes are practically the same. This is understandable, as a representative volume of the crystalline structures includes CNTs in one translation cell, which in stage I includes one CNT and in stage II includes 1×2 CNTs; see the third column of Figure 2. At stage III, the effect of the cell size is noticeable, as the representative volume for an irregular structure containing collapsed CNTs is larger than that for crystalline structures. At stage IV, the compressive stresses increase rapidly with the strain because of the completely collapsed CNTs and the highly dense structure.

It is interesting to discuss the anisotropy of various structures. At stage I, the uniaxial compression produces weakly anisotropic structures with elliptic CNT cross sections and that is why the components of the normal stresses are not equal in Figure 3a, b. The biaxial compression within stage I preserves isotropy and in Figure 3c one has $\sigma_{xx} = \sigma_{yy}$, as already mentioned. The crystalline structures at stage II are anisotropic, and the greatest anisotropy is observed upon compression along the y-axis, because of the largest difference between σ_{xx} and σ_{yy}. The anisotropy at stage II is the weakest for biaxial compression and it is intermediate for compression along the x-axis. The same trend can be seen during stages III and IV. This means that the biaxial compression produces a nearly isotropic CNT bundle with collapsed nanotubes; the compression along the x-axis results in the intermediate anisotropy of the bundle and the compression along the y-axis produces the largest anisotropy. In fact, a close look at the structures presented in the bottom row of Figure 2 reveals that the collapsed CNTs have a preferred horizontal orientation in (k), vertical (but less pronounced) orientation in (j), and that there is no preferred orientation of collapsed CNTs in (l).

3.3. Elastic Constants

In this section, engineering elastic constants are presented for the crystalline structures of the CNT bundles as the functions of volumetric strain. We recall that structures with translational symmetry are observed upon deformation at stages I and II. The elastic constants of the structures observed at stages III and IV are not analyzed, as the size of the computational cell used in our calculations is rather small and does not reflect the mechanical properties of the irregular structures.

The dependence of Poisson's ratios ν_{xy} (the black lines) and ν_{yx} (the blue lines) on $|\theta|$ is shown in **Figure 4** for the cases of: (a) compression along the x-axis, (b) compression along the y-axis, and (c) biaxial compression. The vertical dashed lines separate stage I and stage II. The horizontal dashed lines highlight the zero value of Poisson's ratio.

The analysis of the plots in Figure 4 reveals that within stage I, ν_{xy} and ν_{yx} are almost equal and approach 1 with an increase in $|\theta|$. In (a), however, ν_{yx} is slightly greater than ν_{xy} and in (b) the opposite is true. The equality $\nu_{xy} = \nu_{yx}$ in (c) follows from the isotropy of the structure shown in Figure 2c under biaxial compression. Note that for the isotropic 2D material, the energy conservation law suggests that the Poisson's ratio must be within $-1 \leq \nu \leq 1$.[89] It becomes clear that the reason for the transformation of the structure during the transition from stage I to stage II is the approach of Poisson's ratio to the limiting value of 1.

The Poisson's ratios at stage II differ markedly from those at stage I. A sharp drop of both ν_{xy} and ν_{yx} is observed at the transition point. For all three loading schemes, one of the Poisson's ratios remains positive and the other one becomes negative, which indicates that the structure of the laterally compressed CNT bundle at stage II exhibits partial auxetic properties. For compression along the x-axis, one has $\nu_{xy} < 0$, but for compression along the y-axis and for biaxial compression, $\nu_{yx} < 0$.

T figure out the mechanical behavior of the deformed CNT bundle, in **Figure 5** we analyze the values of tangent Young's moduli E_{xx} and E_{yy} and tangent shear modulus G. Black, red, and blue lines are used for illustrating E_{xx}, E_{yy}, and G, respectively. The vertical dashed line shows the border between stage I and stage II.

At stage I, E_{xx} and E_{yy} grow linearly with an increase in $|\theta|$ for all three loading schemes. The tangent shear modulus G also increases with compressive strain but remains 4–5 times smaller than the tangent Young's moduli. Transition from stage

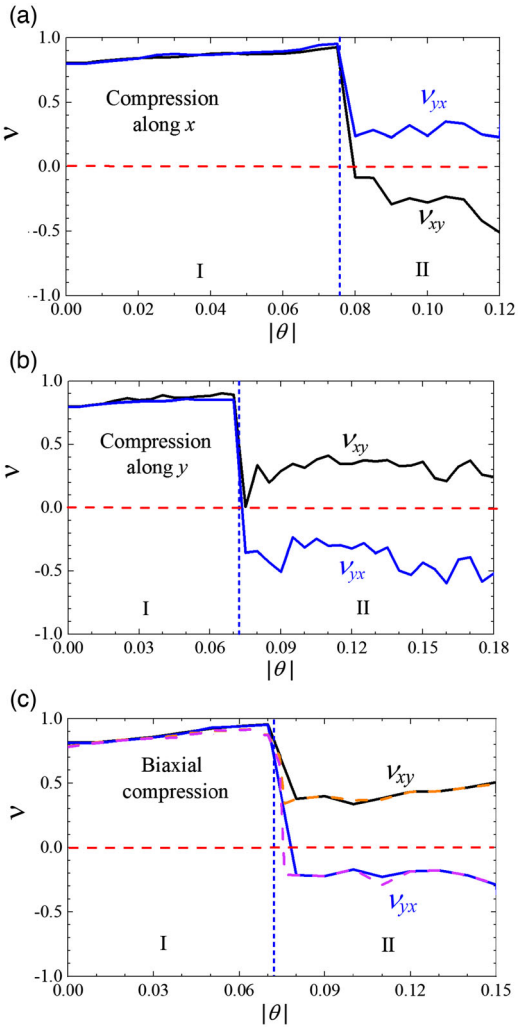

Figure 4. a–c) Poisson's ratios as the functions of the volumetric compressive strain during compression along the *x*-axis (a), along the *y*-axis (b), and for biaxial compression (c). The black (blue) lines show ν_{xy} (ν_{yx}). Vertical dashed lines separate stage I from stage II. The horizontal dashed line highlights the zero value of Poisson's ratio.

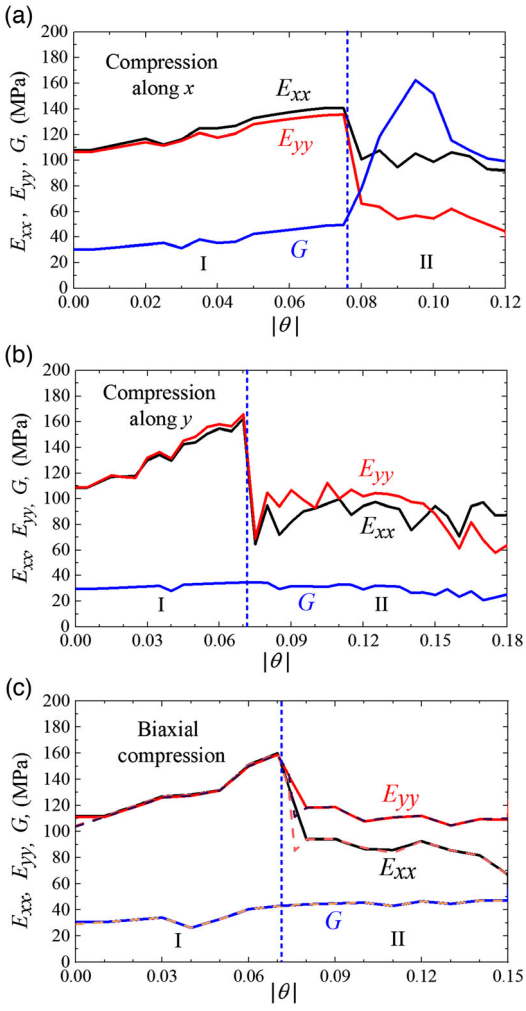

Figure 5. a–c) Tangent Young's moduli and tangent shear modulus for compression along the *x*-axis (a), along the *y*-axis (b), and for biaxial compression (c). The black (red) lines show E_{xy} (E_{yy}) and the blue line is for the tangent shear modulus G. The vertical dashed lines separate stage I from stage II.

I to stage II results in a sharp drop of the tangent Young's moduli. After drop, at stage II, E_{xx} is greater than E_{yy} in the case of compression along the *x*-axis, E_{xx} and E_{xx} are about the same for compression along the *y*-axis, and E_{xx} is smaller than E_{yy} for biaxial compression.

We turn to the discussion of the tangent shear modulus at stage II. For compression along the *y*-axis and biaxial compression, as shown in Figure 5b,c, the tangent shear modulus remains almost constant within the stage II and there is no a change of the share modulus at the transition from stage I to stage II. This means that the structures with the doubled translational cell shown in Figure 2e,f have the same shear rigidity as the structures in Figure 2b,c. A completely different behavior of G is observed for compression along the *x*-axis, see Figure 5a. As soon as the border between the stage I and stage II is crossed, G starts to increase with $|\theta|$ and soon it becomes greater than the tangent Young's moduli E_{xx} and E_{yy}. The increase in G can be attributed to the formation of a special pattern of elliptic CNTs with four nanotubes in a translational cell, see 2(d), which counteracts shear deformation.

3.4. Deformation Mechanisms

Figure 6 shows the displacement vectors of the centers of gravity of CNTs' cross sections. The left (right) column gives the results for $|\theta| = 0.2$ ($|\theta| = 0.3$). The first, second, and third rows display the results for the compression along the *x*-axis, biaxial compression, and compression along the *y*-axis, respectively. The line segments connect the centers of gravity of CNTs in the uniformly deformed structure with the current positions shown by the dots. Recall that the actual CNT bundle structures at $|\theta| = 0.3$ are shown in the bottom row of Figure 2 and here they correspond to the right column.

The results shown in Figure 6 suggest that the strain-induced displacements of CNTs' centers of gravity depend considerably

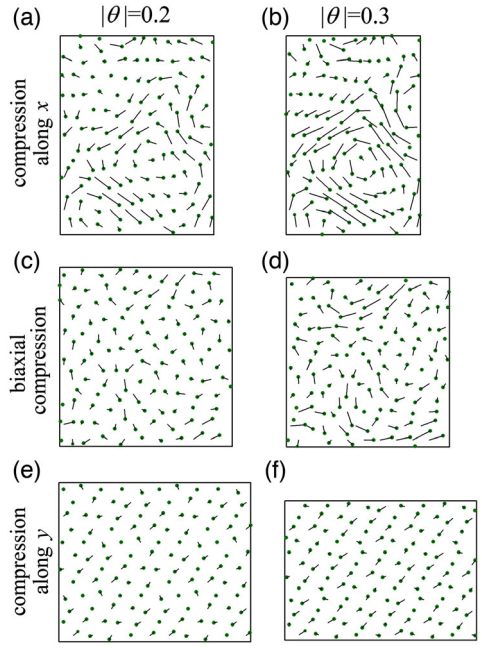

Figure 6. Displacement vectors of the CNTs' centers of gravity at $|\theta| = 0.2$ (the left column) and $|\theta| = 0.3$ (the right column). In the first, second, and third rows, results for the compression along the *x*-axis, biaxial compression, and compression along the *y*-axis, respectively, are presented. The dots show the current positions of the centers of gravity. The line segments connect the positions of the centers of gravity in the uniformly deformed structure with the current positions.

on the deformation scheme. Thus, in case of compression along the *x*-axis (along a close-packed direction), vortex patterns of the displacement vectors can be seen (the first row of Figure 6). For the case of compression along the *y*-axis (normal to a close-packed direction), the displacement vectors are much shorter and do not produce vortexes (the bottom row of Figure 6). In (a) and (b), the length of many displacement vectors exceeds the distance between neighboring CNTs, but in (e) and (f), the length of the displacement vectors is smaller than this distance. The length for the case of biaxial compression, shown in (c) and (d), is naturally between those in the two uniaxial compression schemes.

It can be concluded that, upon the uniaxial compression of the CNT bundle in the direction of close packing, the CNT collapse is accompanied by noticeable vortex-like displacements of the centers of gravity. In contrast, the main mechanism of compression deformation perpendicular to the direction of close packing is the collapse of CNTs with relatively small displacements.

4. Discussion and Conclusion

The elastic properties of a CNT bundle were analyzed under plain strain lateral compression using perturbation–relaxation MD in the framework of the chain model with a reduced number of degrees of freedom. The uniaxial compression along the direction of close packing (the *x*-axis) and normal to it (the *y*-axis), as well as the biaxial compression, were analyzed.

For all the loading schemes, the stress–strain curves can be divided into four stages; see Figure 3.

Stage I: Slightly deformed CNTs form crystalline structures with a single CNT in translation cell, see Figure 2a–c. In (a) and (b), CNTs have elliptic cross sections elongated along the vertical and horizontal directions, respectively, whereas in (c) slightly polygonized CNTs are observed. The compressive stress components grow rapidly with the strain, see Figure 3.

Stage II: CNTs having elliptic cross sections form crystalline structures with doubled translation cells, see Figure 2d–f. In (d), the translation cell includes four CNTs and in (e) and (f) the cell includes two CNTs. Transition from stage I to stage II results in a sharp change of the slope of the stress–strain curves, and within stage II, the compressive stress components change linearly with the strain, see Figure 3.

Stage III: Collapsed CNTs appear in the structure and the fraction of the collapsed CNTs increases with the increased compressive strain, see Figure 2g,j–l. Transition from stage II to stage III results in a sharp drop of the compressive stresses. In stage III, the compressive stresses change slowly with the strain, see Figure 3.

Stage IV: All CNTs collapse. The compressive stresses grow very rapidly with the deformation, as there is no free volume in the system, see Figure 3.

The following new results were obtained. 1) Engineering elastic constants for the CNT bundle under lateral compression were calculated as the functions of the volumetric strain for stages I and II. Poisson's ratios ν_{xy} and ν_{yx} are shown in Figure 4, whereas Young's moduli E_{xx}, E_{yy}, and shear modulus G are shown in Figure 5. The CNT bundle exhibits very unusual elastic properties, as described later. 2) Within stage I, the bundle has Poisson's ratios close to 1 and approach 1 with increasing compressive volumetric strain, see Figure 4. For an isotropic 2D elastic material, the Poisson's ratio cannot exceed 1, as the instability of the structure with a single CNT inside the translation cell arises when the Poisson's ratio approaches 1. A transition to a structure with a double translation cell indeed occurs at a volumetric strain of about 7%, see Figure 2. Note that most common crystalline materials have Poisson's ratios in the range from 0.25 to 0.35, so a value close to 1 for an isotropic elastic body (realized in our simulations for biaxial compression within stage I) is exceptionally high. 3) The CNT bundle under compression within stage II exhibits partial auxetic properties, see Figure 4. For the compression along the *x*-axis $\nu_{xy} < 0$ and $\nu_{yx} > 0$, whereas for the compression along the *y*-axis and the biaxial compression, $\nu_{xy} > 0$ and $\nu_{yx} < 0$. 4) Young's moduli and shear modulus grow linearly with the compressive strain within stage I with G being 4−5 times smaller than E_{xx} and E_{yy}, see Figure 5. In stage II, the Young's moduli E_{xx} and E_{yy} are noticeably smaller than those in stage I. The shear modulus in stages I and II is practically the same for compression along the *y*-axis and the uniaxial compression, see Figure 5b,c. However, in the case of the compression along the *x*-axis, in stage II, G is greater than E_{xx} and E_{yy}, see Figure 5a. 5) The compression of the CNT bundle perpendicular to the direction of close packing produces the structure with collapsed CNTs having the highest degree of anisotropy. The biaxial compression produces nearly isotropic structure, and the compression along the close-

packed direction produces the structure with an intermediate degree of anisotropy. Note that the degree of anisotropy can be characterized by the difference in the compressive stress components σ_{xx} and σ_{yy}; see Figure 3. 6) As for the mechanisms of deformation, upon the uniaxial compression of the CNT bundle in the direction of close packing, the CNT collapse is accompanied by noticeable vortex-like displacements of the centers of gravity, see Figure 6a,b. In contrast, the main mechanism of compression deformation perpendicular to the direction of close packing is the collapse of CNTs with very small displacements, see Figure 6e,f.

The auxetic properties of isotropic and orthotropic media with a complex structure can be described within the framework of micropolar continuum models, see various studies.[90–93] The skewed assembly of CNT cross sections observed at stage II (see Figure 2) does not give an equivalent planar special orthotropic continuum, and in this case more complex theories should be developed.

The auxetic behavior observed for the crystal structures of the CNT bundle at stage II cannot be explained by the mechanism of rotating units,[94–97] as no noticeable rotation of the CNT cross sections was found. Partial auxeticity is commonly observed in strongly anisotropic materials.[98,99] The anisotropy of the considered CNT bundle at stage II, in which partial auxeticity is observed, is low and can hardly be the cause of auxetic properties. Possibly, the mechanism of the auxeticity of the CNT bundle as a nanomaterial is similar to those of foam and other similar microscopic and macroscopic structures.[100–103]

Further study on the effect of temperature and arrangement of CNTs on the mechanical properties of the bundle is left for future work. Analyses of complex structures with vortices or crystalline domains are also reserved for future research.

Overall, the obtained data on the structure and elastic properties of CNT bundles upon lateral compression contribute to the understanding of the deformation mechanisms of bundle-type structures and provide guidance for the design of materials with desired mechanical properties.

Acknowledgements

Research of E.G.S. was conducted at Tomsk Polytechnic University within the framework of Tomsk Polytechnic University Competitiveness Enhancement Program grant. S.V.D. acknowledges the support of the Russian Science Foundation grant no. 21-19-00813.

Conflict of Interest

The authors declare no conflict of interest.

Author Contributions

The conceptualization was done by S.A.V. The methodology was done by S.V.D. The software was taken care of E.A.K., L.Kh.R., and A.A.K.Investigation was conducted by L.Kh.R., A.A.K., and E.G.S. Data curation was taken care of by E.A.K. and E.G.S. S.V.D., E.A.K., and K.Z wrote the original draft. All authors have read and agreed to the published version of the manuscript.

Data Availability Statement

The data that support the findings of this study are available on request from the corresponding author. The data are not publicly available due to privacy or ethical restrictions.

Keywords

auxetic, carbon nanotube bundles, chain models, elastic properties, lateral compression

Received: April 4, 2021
Revised: September 1, 2021
Published online:

[1] S. Iijima, *Nature* **1991**, *354*, 56.
[2] R. Zhang, Y. Zhang, F. Wei, *Acc. Chem. Res.* **2017**, *50*, 179.
[3] E. Gao, W. Lu, Z. Xu, *Carbon* **2018**, *138*, 134.
[4] C. S. Haines, N. Li, G. M. Spinks, A. E. Aliev, J. Di, R. H. Baughman, *Proc. Natl. Acad. Sci.* **2016**, *113*, 11709.
[5] M. G. Donato, S. Galvagno, M. Lanza, G. Messina, C. Milone, E. Piperopoulos, A. Pistone, S. Santangelo, *J. Nanosci. Nanotechnol.* **2009**, *9*, 3815.
[6] T. Kaur, M. Kumar Rai, R. Khanna, *Phys. Status Solidi A* **2021**, *218*, 2000588.
[7] D. Appell, *Phys. World* **2011**, *24*, 30.
[8] R. Zhang, Q. Wen, W. Qian, D. S. Su, Q. Zhang, F. Wei, *Adv. Mater.* **2011**, *23*, 3387.
[9] S. H. Kim, C. S. Haines, N. Li, K. J. Kim, T. J. Mun, C. Choi, J. Di, Y. J. Oh, J. P. Oviedo, J. Bykova, S. Fang, N. Jiang, Z. Liu, R. Wang, P. Kumar, R. Qiao, S. Priya, K. Cho, M. Kim, M. S. Lucas, L. F. Drummy, B. Maruyama, D. Y. Lee, X. Lepró, E. Gao, D. Albarq, R. Ovalle-Robles, S. J. Kim, R. H. Baughman, *Science* **2017**, *357*, 773.
[10] Y. Bai, R. Zhang, X. Ye, Z. Zhu, H. Xie, B. Shen, D. Cai, B. Liu, C. Zhang, Z. Jia, S. Zhang, X. Li, F. Wei, *Nat. Nanotechnol.* **2018**, *13*, 589.
[11] J. Di, S. Fang, F. A. Moura, D. S. Galvão, J. Bykova, A. Aliev, M. J. d. Andrade, X. Lepró, N. Li, C. Haines, R. Ovalle-Robles, D. Qian, R. H. Baughman, *Adv. Mater.* **2016**, *28*, 6598.
[12] Y. Li, X. Zhang, X. Tao, J. Xu, W. Huang, J. Luo, Z. Luo, T. Li, F. Liu, Y. Bao, H. J. Geise, *Carbon* **2005**, *43*, 295.
[13] B. Liu, T. Lee, S. Lee, C. Park, C. Lee, *Chem. Phys. Lett.* **2003**, *377*, 55.
[14] E. G. Rakov, *Russ. Chem. Rev.* **2013**, *82*, 538.
[15] A. Karimzad Ghavidel, M. Zadshakoyan, M. Arjmand, *Int. J. Mech. Sci.* **2021**, *196*, 106289.
[16] H. Cho, J. Kim, J. Hwang, C. Kim, S. Jang, C. Park, H. Lee, M. Kim, *Sci. Rep.* **2020**, *10*, 7416.
[17] K. Kaneko, K. Hori, S. Noda, *Carbon* **2020**, *167*, 596.
[18] M. Kim, Y. Lee, J.-H. Oh, S.-H. Hong, B.-I. Min, T.-H. Kim, S. Choi, *Chem. Eng. J.* **2020**, *395*, 125148.
[19] H. Sedighi, H. Ouakad, R. Dimitri, F. Tornabene, *Phys. Scr.* **2020**, *95*, 065204.
[20] S. A. Shcherbinin, K. Zhou, S. V. Dmitriev, E. A. Korznikova, A. R. Davletshin, A. A. Kistanov, *J. Phys. Chem. C* **2020**, *124*, 10235.
[21] S. Shcherbinin, S. Ustiuzhanina, A. Kistanov, *J. Micromech. Mol. Phys.* **2020**, *5*, 2050007.
[22] D. Qian, G. J. Wagner, W. K. Liu, M.-F. Yu, R. S. Ruoff, *Appl. Mech. Rev.* **2002**, *55*, 495.
[23] H. Zhan, G. Zhang, J. M. Bell, V. B. C. Tan, Y. Gu, *Nat. Commun.* **2020**, *11*, 1905.

[24] J. Baimova, S. Dmitriev, K. Zhou, *Phys. Status Solidi B* **2012**, *249*, 1393.
[25] A. Savin, E. Korznikova, A. Krivtsov, S. Dmitriev, *Eur. J. Mech., A/Solids* **2020**, *80*, 103920.
[26] A. Savin, E. Korznikova, S. Dmitriev, *Mech. Mater.* **2019**, *137*, 103123.
[27] A. Savin, E. Korznikova, S. Dmitriev, *Phys. Rev. B* **2015**, *92*, 035412.
[28] A. Savin, R. Sakovich, M. Mazo, *Phys. Rev. B* **2018**, *97*, 165436.
[29] J. A. Elliott, J. K. W. Sandler, A. H. Windle, R. J. Young, M. S. P. Shaffer, *Phys. Rev. Lett.* **2004**, *92*, 095501.
[30] Y. Cheng, N. Maria Pugno, X. Shi, B. Chen, H. Gao, *J. Appl. Mech.* **2013**, *80*, 040902.
[31] S. Silva-Santos, R. Alencar, A. Aguiar, Y. Kim, H. Muramatsu, M. Endo, N. Blanchard, A. San-Miguel, A. Souza Filho, *Carbon* **2019**, *141*, 568.
[32] X. Zhang, in *Nanomechanics* (Ed: A. Vakhrushev), InTech, Rijeka, Croatia **2017**, pp. 1–29.
[33] R. Alencar, W. Cui, A. Torres-Dias, T. F. Cerqueira, S. Botti, M. A. Marques, O. Ferreira, C. Laurent, A. Weibel, D. Machon, D. J. Dunstan, A. G. Souza Filho, A. San-Miguel, *Carbon* **2017**, *125*, 429.
[34] C.-C. Lee, P.-C. Huang, *Comput. Model. Eng. Sci.* **2019**, *120*, 239.
[35] C.-C. Lee, N.-T. Tsou, T.-S. Kim, *Comput. Model. Eng. Sci.* **2019**, *120*, 235.
[36] Q. Wang, V. K. Varadan, *Smart Mater. Struct.* **2005**, *14*, 281.
[37] M. Wang, X. Qiu, X. Zhang, *Nanotechnology* **2007**, *18*, 075711.
[38] H. Shima, M. Sato, *Nanotechnology* **2008**, *19*, 495705.
[39] M. Wang, X. Zhang, Q. Zheng, Y. Liu, *Nanotechnology* **2007**, *18*, 375706.
[40] Y. Li, X. Qiu, F. Yang, X.-S. Wang, Y. Yin, *Nanotechnology* **2008**, *19*, 165502.
[41] Y. Li, X. Qiu, F. Yang, X.-S. Wang, Y. Yin, *Nanotechnology* **2008**, *19*, 225701.
[42] N. Gupta, J. Alred, E. Penev, B. Yakobson, *ACS Nano* **2021**, *15*, 1342.
[43] V. Coluci, N. Pugno, S. Dantas, D. Galvão, A. Jorio, *Nanotechnology* **2007**, *18*, 335702.
[44] I. Evazzade, I. Lobzenko, O. Golubev, E. Korznikova, *J. Micromech. Mol. Phys.* **2020**, *5*, 2050001.
[45] D. Mähnlich, O. Eberhardt, T. Wallmersperger, *Acta. Mech.* **2020**, *232*, 483.
[46] A. Savin, M. Mazo, *Phys. Solid State* **2018**, *60*, 826.
[47] A. V. Savin, E. A. Korznikova, S. V. Dmitriev, *Phys. Solid State* **2015**, *57*, 2348.
[48] A. Savin, E. Korznikova, S. Dmitriev, E. Soboleva, *Comput. Mater. Sci.* **2017**, *135*, 99.
[49] E. Korznikova, L. Rysaeva, A. Savin, E. Soboleva, E. Ekomasov, M. Ilgamov, S. Dmitriev, *Materials* **2019**, *12*, 3951.
[50] L. K. Rysaeva, E. A. Korznikova, R. T. Murzaev, D. U. Abdullina, A. A. Kudreyko, J. A. Baimova, D. S. Lisovenko, S. V. Dmitriev, *Facta Univ., Ser.: Mech. Eng.* **2020**, *18*, 1.
[51] D. U. Abdullina, E. A. Korznikova, V. I. Dubinko, D. V. Laptev, A. A. Kudreyko, E. G. Soboleva, S. V. Dmitriev, K. Zhou, *Computation* **2020**, *8*, 27.
[52] L. K. Rysaeva, D. V. Bachurin, R. T. Murzaev, D. U. Abdullina, E. A. Korznikova, R. R. Mulyukov, S. V. Dmitriev, *Facta Univ., Ser.: Mech. Eng.* **2020**, *18*, 525.
[53] A. Savin, E. Korznikova, S. Dmitriev, *Phys. Rev. B* **2019**, *99*, 235411.
[54] S. V. Dmitriev, A. S. Semenov, A. V. Savin, M. A. Ilgamov, D. V. Bachurin, *J. Micromech. Mol. Phys.* **2020**, *5*, 2050010.
[55] S. V. Dmitriev, I. R. Sunagatova, M. A. Ilgamov, I. S. Pavlov, *Tech. Phys.* **2021**, *91*, 1732.
[56] K. Dudek, D. Attard, R. Caruana-Gauci, K. Wojciechowski, J. Grima, *Smart Mater. Struct.* **2016**, *25*, 025009.
[57] K. Dudek, R. Gatt, L. Mizzi, M. Dudek, D. Attard, K. Evans, J. Grima, *Sci. Rep.* **2017**, *7*, 46529.
[58] R. Gatt, L. Mizzi, J. Azzopardi, K. Azzopardi, D. Attard, A. Casha, J. Briffa, J. Grima, *Sci. Rep.* **2015**, *5*, 8395.
[59] K. Alderson, A. Alderson, J. Grima, K. Wojciechowski, *Phys. Status Solidi B* **2014**, *251*, 263.
[60] V. Ho, D. Ho, S.-Y. Kwon, S. Kim, *Phys. Status Solidi B* **2016**, *253*, 1303.
[61] M. Terrones, F. Banhart, N. Grobert, J.-C. Charlier, H. Terrones, P. Ajayan, *Phys. Rev. Lett.* **2002**, *89*, 075505.
[62] J. Romo-Herrera, M. Terrones, H. Terrones, S. Dag, V. Meunier, *Nano Lett.* **2007**, *7*, 570.
[63] G. Dimitrakakis, E. Tylianakis, G. Froudakis, *Nano Lett.* **2008**, *8*, 3166.
[64] Y. Li, X. Qiu, F. Yang, Y. Yin, Q. Fan, *Carbon* **2009**, *47*, 812.
[65] Y. Sun, N. Pugno, *Materials* **2013**, *6*, 699.
[66] A. Pedrielli, S. Taioli, G. Garberoglio, N. Pugno, *Carbon* **2017**, *111*, 796.
[67] J. Grima, S. Winczewski, L. Mizzi, M. Grech, R. Cauchi, R. Gatt, D. Attard, K. Wojciechowski, J. Rybicki, *Adv. Mater.* **2015**, *27*, 1455.
[68] F. Scarpa, J. Narojczyk, K. Wojciechowski, *Phys. Status Solidi B* **2011**, *248*, 82.
[69] L. Hall, V. Coluci, D. Galvão, M. Kozlov, M. Zhang, S. Dantas, R. Baughman, *Science* **2008**, *320*, 504.
[70] V. Coluci, L. Hall, M. Kozlov, M. Zhang, S. Dantas, D. Galvão, R. Baughman, *Phys. Rev. B* **2008**, *78*, 115408.
[71] S. Patole, M. Arif, R. Susantyoko, S. Almheiri, S. Kumar, *Sci. Rep.* **2018**, *8*, 12188.
[72] L. Rysaeva, J. Baimova, S. Dmitriev, D. Lisovenko, V. Gorodtsov, A. Rudskoy, *Diamond Relat. Mater.* **2019**, *97*, 107411.
[73] L. Rysaeva, J. Baimova, D. Lisovenko, V. Gorodtsov, S. Dmitriev, *Phys. Status Solidi B* **2019**, *256*, 1800049.
[74] D. Lisovenko, J. Baimova, L. Rysaeva, V. Gorodtsov, A. Rudskoy, S. Dmitriev, *Phys. Status Solidi B* **2016**, *253*, 1295.
[75] Y. Chandra, F. Scarpa, S. Adhikari, J. Zhang, E. Saavedra Flores, H.-X. Peng, *Compos. Part B: Eng.* **2016**, *102*, 1.
[76] E. Randjbaran, D. L. Majid, R. Zahari, M. T. H. Sultan, N. Mazlan, *Facta Univ. Ser. Mech. Eng.* **2020**, *18*, 229.
[77] Y. Li, S. Luo, M.-C. Yang, R. Liang, C. Zeng, *Adv. Funct. Mater.* **2016**, *26*, 2900.
[78] L. Valentini, S. Bittolo Bon, N. Pugno, *Adv. Funct. Mater.* **2017**, *27*, 1606526.
[79] S. Yuan, C. Chua, K. Zhou, *Adv. Mater. Technol.* **2019**, *4*, 1800419.
[80] R. Goldstein, V. Gorodtsov, D. Lisovenko, M. Volkov, *Smart Mater. Struct.* **2016**, *25*, 054006.
[81] C. Luo, C. Han, X. Zhang, X. Zhang, X. Ren, Y. Xie, *Thin-Walled Struct.* **2021**, *163*, 107682.
[82] R. Goldstein, V. Gorodtsov, D. Lisovenko, *Acta Mech.* **2018**, *229*, 2189.
[83] R. Goldstein, V. Gorodtsov, D. Lisovenko, M. Volkov, *Phys. Status Solidi B* **2015**, *252*, 1580.
[84] G. Van Lier, C. Van Alsenoy, V. Van Doren, P. Geerlings, *Chem. Phys. Lett.* **2000**, *326*, 181.
[85] J. Zhang, D. Jiang, F. Scarpa, H.-X. Peng, *Compos. Part A: Appl. Sci. Manuf.* **2013**, *55*, 188.
[86] F. Scarpa, S. Adhikari, C. Wang, *Int. J. Smart Nano Mater.* **2010**, *1*, 83.
[87] M. Motta, A. Moisala, I. Kinloch, A. Windle, *Adv. Mater.* **2007**, *19*, 3721.
[88] S. V. Dmitriev, E. A. Korznikova, D. I. Bokij, K. Zhou, *Phys. Status Solidi B* **2016**, *253*, 1310.
[89] K. Wojciechowski, *J. Phys. Soc. Jpn.* **2003**, *72*, 1819.
[90] A. Vasiliev, I. Pavlov, *Mech. Res. Commun.* **2021**, *115*, 103732.
[91] Y. Chen, X. Liu, G. Hu, C. *R. Mec* **2014**, *342*, 273.
[92] A. Spadoni, M. Ruzzene, *J. Mech. Phys. Solids* **2012**, *60*, 156.

[93] X. Liu, G. Huang, G. Hu, *J. Mech. Phys. Solids* **2012**, *60*, 1907.
[94] J. Grima, K. Evans, *J. Mater. Sci. Lett.* **2000**, *19*, 1563.
[95] Y. Ishibashi, M. Iwata, *J. Phys. Soc. Jpn.* **2000**, *69*, 2702.
[96] A. A. Vasiliev, S. V. Dmitriev, Y. Ishibashi, T. Shigenari, *Phys. Rev. B* **2002**, *65*, 094101.
[97] J. N. Grima, A. Alderson, K. E. Evans, *Phys. Status Solidi B* **2005**, *242*, 561.
[98] H. Tanaka, K. Suga, N. Iwata, Y. Shibutani, *Sci. Rep.* **2017**, *7*, 39816.
[99] E. H. Harkati, A. Bezazi, W. Boukharouba, F. Scarpa, *Phys. Status Solidi B* **2009**, *246*, 2111.
[100] S. Shan, S. Kang, Z. Zhao, L. Fang, K. Bertoldi, *Extreme Mech. Lett.* **2015**, *4*, 96.
[101] J. Qiao, C. C. Qing, *J. Appl. Mech.* **2015**, *82*, 051007.
[102] A. T. Barnes, K. Ravi-Chandar, S. Kyriakides, S. Gaitanaros, *Int. J. Solids Struct.* **2013**, *51*, 1631.
[103] A. T. Barnes, S. Kyriakides, *Int. J. Solids Struct.* **2013**, *51*, 1646.